Electron-helium *S*-wave model benchmark calculations. I. Single ionization and single excitation

Philip L. Bartlett[1,*] and Andris T. Stelbovics[2,†]
[1]*Centre for Antimatter-Matter Studies, Murdoch University, Perth 6150, Australia*
[2]*Centre for Antimatter-Matter Studies, Curtin University, Perth 6102, Australia*
(Received 3 November 2009; published 18 February 2010)

A full four-body implementation of the propagating exterior complex scaling (PECS) method [J. Phys. B **37**, L69 (2004)] is developed and applied to the electron-impact of helium in an *S*-wave model. Time-independent solutions to the Schrödinger equation are found numerically in coordinate space over a wide range of energies and used to evaluate total and differential cross sections for a complete set of three- and four-body processes with benchmark precision. With this model we demonstrate the suitability of the PECS method for the complete solution of the full electron-helium system. Here we detail the theoretical and computational development of the four-body PECS method and present results for three-body channels: single excitation and single ionization. Four-body cross sections are presented in the sequel to this article [Phys. Rev. A **81**, 022716 (2010)]. The calculations reveal structure in the total and energy-differential single-ionization cross sections for excited-state targets that is due to interference from autoionization channels and is evident over a wide range of incident electron energies.

DOI: 10.1103/PhysRevA.81.022715 PACS number(s): 34.80.Dp

I. INTRODUCTION

The impact of electrons with helium atoms is one of the most intensely studied atomic interactions, both experimentally and theoretically. With its relatively simple electronic structure helium has been invaluable for developing our knowledge of few-body atomic interactions. As an inert atomic gas at room temperature, it is also particularly amenable to high-precision measurement, and electron-impact collisions with its two valence electrons provide a rich set of three- and four-body interaction channels. Three-body interactions include elastic, single-excitation, and single-ionization collisions that are readily modelled with frozen-core methods. Four-body channels consist of excitation to short-lifetime doubly excited (autoionizing) states, single ionization that leaves the remaining He^+ ion in an excited state (that subsequently decays by photon emission), and double ionization or complete breakup of the target. While helium is eminently suitable for measurement, it is the four-body channels that pose the most significant obstacle to the complete theoretical modeling of *e*-He interactions. Though significant progress has been made in recent years, four-body processes are yet to be *completely* and accurately described at low-to-moderate energies with any nonperturbative *ab initio* method. This has provided the motivation to develop a four-body implementation of the propagating exterior complex scaling (PECS) method [1,2] that can accurately calculate all channels open to the *e*-He system.

Many nonperturbative methods have successfully calculated *e*-He three-body cross sections, including convergent close coupling (CCC) [3], *R* matrix with pseudostates (RMPS) [4], and time-dependent close coupling (TDCC) [5]. All these methods use a frozen-core approximation where the incoming electron interacts with a single valence electron surrounding a He^+ core, forming a pseudo three-body system. The elastic, single-excitation, and single-ionization cross sections and spin asymmetry parameters calculated by these methods are generally in very good agreement with measurements. However, by the nature of the frozen-core approximation four-body processes cannot be calculated, nor indeed any interference phenomena in the three-body channels that are caused by four-body processes. More recently the CCC method has been extended by relaxing the frozen-core approximation, in a model calculation [6], to permit the possibility of final states with the core electron excited to a few low-level states. This relaxed frozen-core approach has permitted CCC to be applied to the consideration of ionization-with-excitation processes.

To date, TDCC is the only nonperturbative *ab initio* four-body technique that has been used to successfully calculate total double-ionization cross sections for helium at low energies [7]. Recent TDCC calculations [8] also give energy- and angle-differential results for double ionization but they disagree markedly with measurements, while their shape is in general agreement for some kinematic arrangements. Many four-body processes such as double excitation and ionization with excitation are yet to be explored with this method, so the electron-helium system remains only partially solved. Given the kinematically complete "reaction microscope" measurements [9,10] for helium that have been performed recently, the demand for accurate theoretical modeling of four-body processes is increasing.

An *S*-wave model for *e*-He has been used in the last decade as a test bed for new four-body computational methods. The TDCC [11], time-independent CCC [6,12], and time-dependent exterior complex scaling (TD-ECS) [13,14] methods have been applied to this model problem, which is similar to the Temkin-Poet [15,16] model for electron-hydrogen collisions. The model maintains all of the characteristics of the full problem but with a significantly lower computation overhead by retaining only a single partial wave (where all angular momenta are zero) from a full partial-wave expansion of the system. While all of these *S*-wave implementations are

*p.bartlett@murdoch.edu.au
†a.stelbovics@curtin.edu.au

in good agreement (especially the comprehensive calculations undertaken using CCC and TD-ECS), it is interesting to note that even for this simplified model problem not all four-body channels have been accurately described, and no method has presented differential cross sections for four-body processes.

In Sec. II we detail the theoretical and computational development of the four-body time-independent PECS method that provides a complete solution for e-He S-wave model collisions with benchmark precision. This method uses the same exterior complex scaling transformation that was pioneered by McCurdy, Rescigno, and co-workers [17,18] for the electron-hydrogen system and more recently applied to the same S-wave model [13], though in a time-dependent formulation. For the e-H system, the PECS propagation algorithms proved to be highly efficient and provided *ab initio* benchmark results for a large range of impact energies, including the notoriously difficult near-threshold region [19–21]. Further refinements to the propagation and computational algorithms are presented here that provide very significant improvements to the computational efficiency of this four-body implementation of PECS. Atomic units are used throughout these derivations. In Sec. III we present elastic, single-excitation, energy-differential ionization, and total ionization cross sections for ground-state and excited-state targets with projectile energies ranging between 5 and 500 eV. Cross sections for the four-body channels of these targets are presented in the sequel to this article [22].

II. THEORY

A. Scattering wave function

The PECS method for electron-helium collisions developed here calculates the scattering wave functions directly on a numerical mesh in coordinate space using the time-independent Schrödinger equation. Near the outer boundary of the mesh the exterior complex scaling (ECS) transformation

$$r \mapsto \begin{cases} r, & r < R_0 \\ R_0 + (r - R_0)e^{i\theta}, & r \geqslant R_0 \end{cases} \tag{1}$$

is used to rotate the radial contours by the angle θ into the complex plane, where R_0 is selected to be sufficiently large to ensure the wave function approaches its asymptotic form near R_0. Beyond R_0 outgoing waves are exponentially damped, allowing the boundary conditions to be approximated by zero. Thus, numerical solutions are evaluated without explicit knowledge of the boundary conditions at the outer edges of the numerical mesh. The theoretical justification for this method, in its application to ionizing collisions, was developed in a series of articles by McCurdy, Rescigno, and co-workers [17,23,24].

The outgoing wave function $\boldsymbol{\Psi}_i^{(+)}$ is separated into an incident $\boldsymbol{\Phi}_i$ and a scattering $\boldsymbol{\Psi}_i$ wave function, related by

$$\boldsymbol{\Psi}_i^{(+)}(0,1,2) = \boldsymbol{\Psi}_i(0,1,2) + \boldsymbol{\Phi}_i(0,1,2), \tag{2}$$

where $n \equiv (\boldsymbol{r}_n, \sigma_n)$ represents the radial and spin coordinates of electron n. The initial state of the system is given by the subscript i and represents the momentum of the incident electron $\boldsymbol{k}_i$ and the energy ϵ_i and initial state $|l_i m_{l_i} s_i m_{s_i}\rangle$ of the target.

As total spin is conserved, the spin and space coordinates may be decoupled using the relation

$$\boldsymbol{\Psi}_i^{SM_S(+)}(0,1,2) = \sum_{s_{12}} \boldsymbol{\Psi}_{i,s_{12}}^{SM_S(+)}(\boldsymbol{r}_0, \boldsymbol{r}_1, \boldsymbol{r}_2)\chi_{s_{12}SM_S}(\sigma_0, \sigma_1, \sigma_2), \tag{3}$$

where S is the total spin angular momentum, M_S is its magnetic substate, and s_{12} is the spin angular momentum of an arbitrary two-electron substate for which electrons 1 and 2 are used throughout these derivations. After decoupling, the scattering wave functions for each S are solved independently, while s_{12} substates of each S are solved simultaneously in our implementation.

By combining the aforementioned relations, the time-independent Schrödinger equation for electron-helium scattering becomes

$$(E - \boldsymbol{H}) \sum_{s_{12}} \boldsymbol{\Psi}_{i,s_{12}}^{SM_S}(\boldsymbol{r}_0, \boldsymbol{r}_1, \boldsymbol{r}_2)\chi_{s_{12}SM_S}(\sigma_0, \sigma_1, \sigma_2) = (\boldsymbol{H} - E)\mathcal{A}\boldsymbol{\Phi}_i^{SM_S}(\boldsymbol{r}_0, \boldsymbol{r}_1, \boldsymbol{r}_2)\chi_{s_i SM_S}(\sigma_0, \sigma_1, \sigma_2), \tag{4}$$

where $\boldsymbol{H}$ is the Hamiltonian operator and E is the total energy of the system. In ECS-based methods the right-hand side (RHS) of Eq. (4) is evaluated numerically. This gives an inhomogeneous differential equation that, after the application of the ECS transformation (1), can be solved numerically on a finite mesh with boundary conditions equal to zero. The antisymmetrization operator on the RHS of (4) ensures that the scattering wave function is antisymmetric with respect to (w.r.t.) exchange of any two electrons.

In electron-helium scattering the target nucleus is sufficiently massive relative to the incident electron that it may be considered fixed in space; thus the Hamiltonian operator used in this derivation is

$$\boldsymbol{H} = \sum_{i=0}^{2} \left(-\frac{1}{2}\nabla_i^2 - \frac{Z}{r_i} + \sum_{j>i}^{2} \frac{1}{|\boldsymbol{r}_i - \boldsymbol{r}_j|} \right), \tag{5}$$

where Z is the nuclear charge.

The S-wave model developed here is similar to the Temkin-Poet [15,16] model for electron-hydrogen collisions and is derived simply by undertaking a full partial-wave expansion of (4) using

$$\boldsymbol{\Psi}_{i,s_{12}}^{SM_S}(\boldsymbol{r}_0, \boldsymbol{r}_1, \boldsymbol{r}_2) = \frac{1}{r_0 r_1 r_2} \sum_{\substack{l_0 l_1 l_2 \\ l_{12} L M_L}} \psi_{i,l_0(l_1 l_2)l_{12}s_{12}}^{LM_L SM_S \Pi}(r_0, r_1, r_2)\mathcal{Y}_{l_0(l_1 l_2)l_{12}}^{LM_L}(\hat{\boldsymbol{r}}_0, \hat{\boldsymbol{r}}_1, \hat{\boldsymbol{r}}_2) \tag{6}$$

and retaining only the partial wave where all angular momenta are zero ($l_0 = l_1 = l_2 = l_{12} = L = 0$). In this expansion, $\mathcal{Y}_{l_0(l_1 l_2)l_{12}}^{LM_L}$ is a tripolar spherical harmonic function with a (arbitrarily chosen) coupling scheme given by $\boldsymbol{l}_{12} = \boldsymbol{l}_1 + \boldsymbol{l}_2$ and $\boldsymbol{L} = \boldsymbol{l}_0 + \boldsymbol{l}_{12}$, where $\boldsymbol{l}_n$ are the angular momenta of each electron.

The initial-state wave function in (4) comprises an incoming Coulomb wave, representing the incident electron (arbitrarily

assigned to r_0) moving in the electrostatic field (charge $Z-2$) of the target, multiplied by the wave function of the target atom (antisymmetric w.r.t. electron exchange),

$$\mathbf{\Phi}_i^{SM_S}(\boldsymbol{r}_0,\boldsymbol{r}_1,\boldsymbol{r}_2)=\mathbf{\Phi}_{\boldsymbol{k}_i,z-2}^{(-)}(\boldsymbol{r}_0)\mathbf{\Phi}_i(\boldsymbol{r}_1,\boldsymbol{r}_2), \tag{7}$$

where we choose the normalization of the Coulomb wave so that

$$\mathbf{\Phi}_{\boldsymbol{k},0}^{(-)}(\boldsymbol{r})=e^{i\boldsymbol{k}\boldsymbol{r}}. \tag{8}$$

For a neutral target ($Z=2$) the Coulomb wave reduces to a plane wave and the full S-wave model expansion for an arbitrary spin state $\chi_{s_{12}SM_S}$ becomes

$$(E-H)\psi_{i,s_{12}}^{SM_S}(r_0,r_1,r_2)=\xi_{i,s_{12}}^{SM_S}(r_0,r_1,r_2) \tag{9}$$

and

$$\begin{aligned}\xi_{i,s_{12}}^{SM_S}&(r_0,r_1,r_2)\\&=\frac{2\sqrt{\pi}}{\sqrt{3}k_i}\big[\xi_i(r_0,r_1,r_2)\delta_{s_is_{12}}-\alpha_{01}^{s_is_{12}S}\xi_i(r_1,r_0,r_2)\\&\quad-\alpha_{02}^{s_is_{12}S}\xi_i(r_2,r_1,r_0)\big],\end{aligned} \tag{10}$$

where

$$\begin{aligned}H=&-\frac{1}{2}\frac{\partial}{\partial r_0}-\frac{1}{2}\frac{\partial}{\partial r_1}-\frac{1}{2}\frac{\partial}{\partial r_2}-\frac{2}{r_0}-\frac{2}{r_1}-\frac{2}{r_2}\\&+\frac{1}{r_{>01}}+\frac{1}{r_{>02}}+\frac{1}{r_{>12}},\end{aligned} \tag{11}$$

$$\xi_i(r_a,r_b,r_c)=\left(\frac{1}{r_{>ab}}+\frac{1}{r_{>ac}}-\frac{2}{r_a}\right)\sin(k_ir_a)\phi_i(r_b,r_c), \tag{12}$$

$$r_{>ab}=\max(r_a,r_b), \tag{13}$$

and $\phi_i(r_b,r_c)$ is the radial part of the S-wave helium wave function for the initial target state i that is antisymmetric w.r.t. electron exchange. The α factors for antisymmetrization are given in the Appendix.

B. Helium wave function

An S-wave approximation of the wave function for the initial i or final j states of the helium target is required when evaluating Eqs. (12) and (26). When evaluating scattering amplitudes of doubly excited (autoionizing) states for e-He collisions it is necessary to use a complex-energy formulation of the helium wave functions. The imaginary part of the energy is inversely proportional to the lifetime of the state and we can see from Table I that the imaginary parts for triplet states are much smaller (and hence longer-lived) than singlet doubly excited states. It is not possible to obtain converged energies, wave functions, or scattering amplitudes for the doubly excited states unless a complex-energy method is used. This is discussed further in the sequel to this article [22].

The helium wave functions were calculated by diagonalizing a target Hamiltonian constructed from finite-difference equations on a numerical mesh and using exterior complex scaling ($R_0=70$ a.u.) to damp the outgoing waves associated with the doubly excited and continuum states of helium. The energies are in excellent agreement with those presented in [14] (to five significant digits for the real part, four significant digits for the imaginary part) and similar agreement with the older calculations of Draeger *et al.* [25] (to five significant digits for bound states, four significant digits for doubly excited states). For interest, we have included a three-dimensional image of the $2s2s^1S$ helium wave function in Fig. 1 that clearly shows the (very slowly) diverging outgoing waves along the axes that are associated with short-lifetime doubly excited states.

TABLE I. Energy levels of selected bound and doubly excited states of helium in the S-wave model.

Helium state	Complex energy (a.u.) Re	Im
$1s1s^1S$	−2.87895	0
$1s2s^3S$	−2.17426	0
$1s2s^1S$	−2.14419	0
$1s3s^3S$	−2.06848	0
$1s3s^1S$	−2.06079	0
$1s4s^3S$	−2.03643	0
$1s4s^1S$	−2.03339	0
$1s5s^3S$	−2.02258	0
$1s5s^1S$	−2.02107	0
$2s2s^1S$	−0.72283	-1.2003×10^{-3}
$2s3s^3S$	−0.58485	-9.0382×10^{-7}
$2s3s^1S$	−0.57192	-2.8488×10^{-4}
$2s4s^3S$	−0.54200	-4.2107×10^{-7}
$2s4s^1S$	−0.53763	-1.1657×10^{-4}

C. Numerical methods

The principle reason for choosing to antisymmetrize the driving term (RHS) of Eq. (4) is to allow the size of the numerical mesh to be reduced and hence improve computational efficiency. By utilizing the known symmetry of the scattering wave functions a triangular pyramidal mesh where $0\leqslant k\leqslant j\leqslant i\leqslant i_{\max}$ (see Fig. 2) may be used instead of a cube. While this requires the simultaneous solution of both s_{12} states, there is still a threefold reduction in the total number of mesh points. The computational effort needed for this

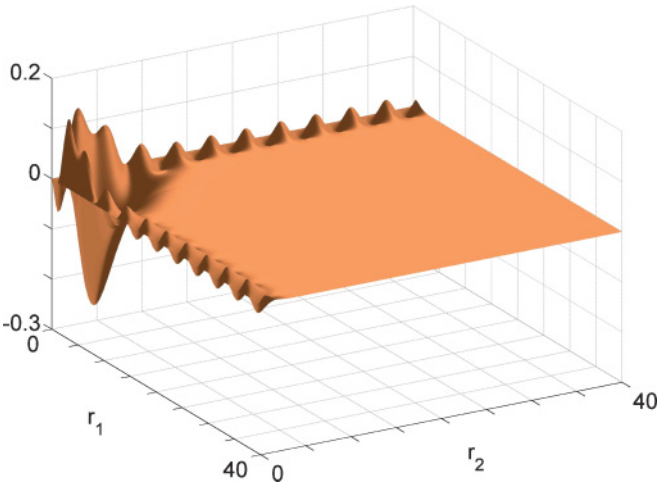

FIG. 1. (Color online) Real part of the helium wave function for the $2s2s^1S$ doubly excited state in the S-wave model. Axes are in atomic units.

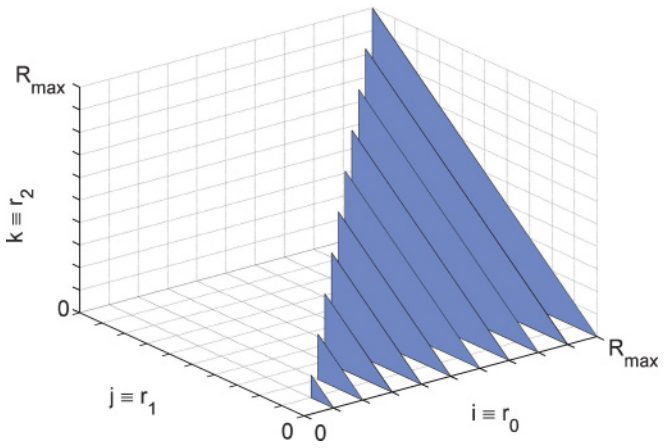

FIG. 2. (Color online) Representation of a triangular pyramidal mesh divided into triangular planes along r_0. Axes are in arbitrary units.

time-independent method scales as approximately $N^{7/3}$, where N is the total number of mesh points, thus antisymmetrization gives a significant computational saving. Also, in contrast to a cubic mesh, the triangular shape allows real-only arithmetic to be used in the real parts of the mesh, providing a further fourfold computational saving in this region.

Rather than solving large and sparse systems of linear equations, the PECS method employs a propagation algorithm that allows the mesh to be divided into a series of planes, where dense linear algebra is used to "solve" each plane separately and the solution is propagated outwards. This is a three-dimensional extension to the PECS method for electron-hydrogen collisions that used a three-point Numerov formula to relate three successive columns of its mesh [2]. While the three-point algorithm is compatible with e-He collisions, very significant savings are made in this PECS implementation by deriving a more accurate Numerov-like formula that relates five sequential points in each dimension. The improved accuracy allows the mesh spacing to be relaxed, offering up to a 50% reduction in the number of mesh points required along each radial dimension. A five-point Numerov formula was derived for the variably spaced (and complex-rotated) mesh that relates each point to its $(5^3 - 1)$ nearest neighbors. The method used to derive these equations is similar to that detailed by Bartlett [2] for e-H collisions, though the significant algebra precludes their inclusion here.

The five-point Numerov method requires the propagation method to be extended to relate five planes of the mesh instead of the three columns used for e-H collisions. This new propagation relation is given by

$$\vec{\psi}^{(i)} = \boldsymbol{P}_1^{(i)}\vec{\psi}^{(i+1)} + \boldsymbol{P}_2^{(i)}\vec{\psi}^{(i+2)} + \vec{V}^{(i)}, \tag{14}$$

where $\boldsymbol{P}_1^{(i)}$ and $\boldsymbol{P}_2^{(i)}$ are two-dimensional propagation matrices and $\vec{V}^{(i)}$ are propagation vectors (introduced to cater for the inhomogeneous term ξ). All the mesh points of $\psi_{i,s_{12}}^{SM_S}$ in the ith plane of the triangular-pyramidal mesh are sequenced into a single vector $\vec{\psi}^{(i)}$. For a five-point Numerov formula the differential Eq. (9) is rearranged into a matrix form,

$$\boldsymbol{A}_{-2}^{(i)}\vec{\psi}^{(i-2)} + \boldsymbol{A}_{-1}^{(i)}\vec{\psi}^{(i-1)} + \boldsymbol{A}_0^{(i)}\vec{\psi}^{(i)} + \boldsymbol{A}_1^{(i)}\vec{\psi}^{(i+1)} + \boldsymbol{A}_2^{(i)}\vec{\psi}^{(i+2)} = \vec{\xi}^{(i)}, \tag{15}$$

where $\boldsymbol{A}_j^{(i)}$, $j \in [-2, 2]$ are a series of sparse two-dimensional matrices containing the Numerov coefficients that relate the points in the $(i + j)$th plane. After two substitutions of (14) into (15) we find the following relations for the propagation matrices and vectors:

$$\boldsymbol{P}_1^{(i)} = -\tilde{\boldsymbol{P}}^{(i)}\boldsymbol{B}^{(i)}, \tag{16}$$

$$\boldsymbol{P}_2^{(i)} = -\tilde{\boldsymbol{P}}^{(i)}\boldsymbol{A}_2^{(i)}, \tag{17}$$

$$\tilde{\boldsymbol{P}}^{(i)} = \left[\left(\boldsymbol{A}_{-2}^{(i)}\boldsymbol{P}_1^{(i-2)} + \boldsymbol{A}_{-1}^{(i)}\right)\boldsymbol{P}_1^{(i-1)} + \left(\boldsymbol{A}_{-2}^{(i)}\boldsymbol{P}_2^{(i-2)} + \boldsymbol{A}_0^{(i)}\right)\right]^{-1}, \tag{18}$$

$$\boldsymbol{B}^{(i)} = \left[\left(\boldsymbol{A}_{-2}^{(i)}\boldsymbol{P}_1^{(i-2)} + \boldsymbol{A}_{-1}^{(i)}\right)\boldsymbol{P}_2^{(i-1)} + \boldsymbol{A}_1^{(i)}\right], \tag{19}$$

$$\vec{\boldsymbol{V}}^{(i)} = \tilde{\boldsymbol{P}}^{(i)}\left[\vec{\xi}^{(i)} - \boldsymbol{A}_{-2}^{(i)}\vec{\boldsymbol{V}}^{(i-2)} - \left(\boldsymbol{A}_{-2}^{(i)}\boldsymbol{P}_1^{(i-2)} + \boldsymbol{A}_{-1}^{(i)}\right)\vec{\boldsymbol{V}}^{(i-1)}\right]. \tag{20}$$

Thus, $\boldsymbol{P}_1^{(i)}$, $\boldsymbol{P}_2^{(i)}$, and $\vec{\boldsymbol{V}}^{(i)}$ are now given in terms of their $(i-1)$ and $(i-2)$ counterparts and form a forward-propagating series. The first plane $(i = 1)$ is calculated using the three-point propagation method (equivalent to setting $\boldsymbol{A}_{-2}^{(i)} = \boldsymbol{A}_2^{(i)} = \boldsymbol{0}$), and $i > 1$ are calculated using the five-point algorithm. Once all propagation matrices and vectors are evaluated, (14) can be evaluated beginning with $i_{\max}$ (where $\vec{\boldsymbol{\psi}}^{(i_{\max})} = \boldsymbol{0}$) and propagated backward. While there is a fourfold increase in the computational effort of this five-plane propagation method over the three-plane method, it is more than compensated by the computational savings of the increased mesh spacing it allows.

In Fig. 3 we present the real part of the scattering wave function of a 150-eV collision with a ground-state target at various r_0. They show the symmetric $(s_{12} = 0)$ and antisymmetric $(s_{12} = 1)$ properties of the wave function w.r.t. exchange of r_1 and r_2, while the r_0 slices show the scattering channels that dominate each region. The distance between peaks of the structures is inversely proportional to the momentum of the outgoing particle(s) in that region. Figures 3(a) and 3(b) at $r_0 = 1$ a.u. have narrow "comb" structures at the edges of the mesh where the elastic scattering process is dominant (superimposed with the smaller contributions from single-excitation channels). The "pond ripple" structure is dominated by single ionization that leaves a ground-state He^+ ion. In Figs. 3(c) and 3(d), where $r_0 = 10$ a.u., the wave function has a significantly smaller magnitude than at 1 a.u., except for the elastic scattering portion at the central peak (this has been truncated so as to emphasize the remaining structures). The "combs" are predominantly a mixture of excitation to higher He singly excited states (inner region) and single ionization (outer region), and the "ripples" correspond to a mixture of ionization-excitation (where the He^+ ion is left in an excited state) and double ionization. Finally, Figs. 3(e) and 3(f) have $r_0 = 35$ a.u. where the "combs" are dominated by single ionization and the "ripples" are mostly double ionization. From these images it is apparent that many of the channels open to the system overlap the same region of coordinate space,

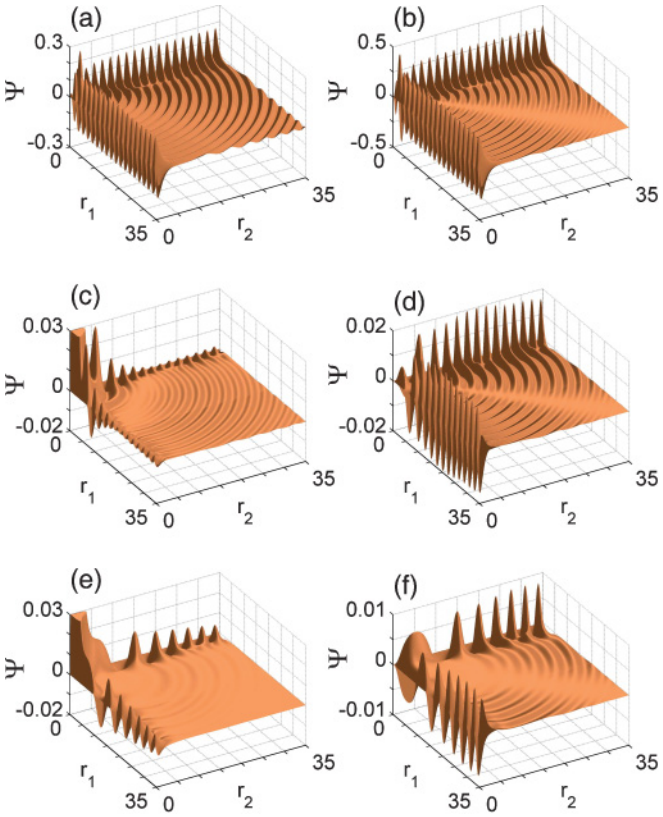

FIG. 3. (Color online) Electron-helium scattering wave function (real part) for $E_0 = 150$ eV at slices taken along $r_0 = 1$, 10, and 35 a.u. (top to bottom). Left column is $s_{12} = 0$ and right column is $s_{12} = 1$. All axes are in atomic units. The central peaks in panels (c) and (e) have been truncated.

which presents the most challenging aspect of the successful extraction of their amplitudes.

D. Scattering amplitude

The scattering amplitudes for electron-helium excitation collisions are evaluated, in a similar manner to the PECS method for electron-hydrogen collisions [2], using an integral described by Peterkop [26]

$$\boldsymbol{I}^S_{ji}(\hat{\boldsymbol{k}}_j) = \int dV \boldsymbol{\Psi}_i^{SM_S(+)}(0,1,2)(\boldsymbol{H}-E)\boldsymbol{\Phi}_{j,\boldsymbol{k}_j}^{SM_S(-)^*}(0,1,2), \tag{21}$$

where $\boldsymbol{\Phi}_{j,\boldsymbol{k}_j}^{SM_S(-)}$ is an asymptotic approximation of the final-state wave function, where j represents the final state of the helium target and $\boldsymbol{k}_j$ is the momentum of the continuum electron in this channel. The volume integral is converted to a surface integral on a hypercube using the divergence theorem, giving

$$\boldsymbol{I}^S_{ji}(\hat{\boldsymbol{k}}_j) \sim \frac{1}{2}\oint \left[\boldsymbol{\Phi}_{j,\boldsymbol{k}_j}^{SM_S(-)^*}(0,1,2)\nabla\boldsymbol{\Psi}_i^{SM_S}(0,1,2) - \boldsymbol{\Psi}_i^{SM_S}(0,1,2)\nabla\boldsymbol{\Phi}_{j,\boldsymbol{k}_j}^{SM_S(-)^*}(0,1,2)\right]dS, \tag{22}$$

and is related to the scattering amplitude by

$$\boldsymbol{I}^S_{ji}(\hat{\boldsymbol{k}}_j) = -2\pi\boldsymbol{F}^S_{ji}(\hat{\boldsymbol{k}}_j). \tag{23}$$

As both the outgoing scattering wave function $\boldsymbol{\Psi}_i^{SM_S(+)}$ and asymptotic final-state wave function $\boldsymbol{\Phi}_{j,\boldsymbol{k}_j}^{SM_S(-)}$ are antisymmetric w.r.t. exchange of any two electrons, the contribution to the scattering amplitude from each of the three surfaces of the hypercube is the same. Therefore, (22) can be evaluated on a single surface as

$$\boldsymbol{F}^S_{ji}(\hat{\boldsymbol{k}}_j) \underset{r_0\to\infty}{\sim} -\frac{3}{4\pi}\int d\hat{\boldsymbol{r}}_0 \int d\boldsymbol{r}_1 \int d\boldsymbol{r}_2 \times \left[\boldsymbol{\Phi}_{j,\boldsymbol{k}_j}^{SM_S(-)^*}(0,1,2)\nabla_0\boldsymbol{\Psi}_i^{SM_S(+)}(0,1,2) - \boldsymbol{\Psi}_i^{SM_S(+)}(0,1,2)\nabla_0\boldsymbol{\Phi}_{j,\boldsymbol{k}_j}^{SM_S(-)^*}(0,1,2)\right], \tag{24}$$

where we have (arbitrarily) chosen to use the surface where $r_0 \to \infty$. On this surface the only term of (the antisymmetrized) $\boldsymbol{\Phi}_{j,\boldsymbol{k}_j}^{SM_S(-)}$ that is asymptotically nonzero is that where r_0 is the coordinate of the continuum electron. Thus the asymptotic final-state is approximated by

$$\boldsymbol{\Phi}_{j,\boldsymbol{k}_j}^{SM_S(-)}(0,1,2) = \frac{1}{\sqrt{3}}\boldsymbol{\Phi}^{(-)}_{\boldsymbol{k}_j,z-2}(\boldsymbol{r}_0)\boldsymbol{\Phi}_j(\boldsymbol{r}_1,\boldsymbol{r}_2)\chi_{s_jSM_S}(\sigma_0,\sigma_1,\sigma_2), \tag{25}$$

where the Coulomb wave reduces to a plane wave for a neutral target.

For the S-wave model with $Z = 2$ the scattering amplitude for non-breakup collisions reduces to

$$F^S_{ji} \underset{r_0\to\infty}{\sim} -\frac{\sqrt{3}}{k_j}\int dr_1 \int dr_2\, \phi_j(r_1,r_2) \times \left[\sin(k_jr_0)\frac{\partial}{\partial r_0}\psi_{i,s_j}^{SM_S}(r_0,r_1,r_2) - \psi_{i,s_j}^{SM_S}(r_0,r_1,r_2)\frac{\partial}{\partial r_0}\sin(k_jr_0)\right], \tag{26}$$

and the total scattering cross section is given by

$$\sigma^S_{ji} = \frac{2S+1}{2(2s_i+1)}\frac{k_j}{k_i}\left|F^S_{ji}\right|^2, \tag{27}$$

where the first term is the spin weighting factor. It is evident from (26) that on the surface used for this integral the only radial scattering wave function that contributes to the scattering amplitude is that where s_{12} matches the spin of the final state s_j. This is not the case if a different surface of the hypercube is chosen.

E. Ionization amplitude

The Peterkop [26] integral is also used to evaluate single-ionization amplitudes,

$$\boldsymbol{I}^S_{ji}(\boldsymbol{k}_1,\boldsymbol{k}_2) = \int dV \boldsymbol{\Psi}_i^{SM_S(+)}(0,1,2)(\boldsymbol{H}-E) \times \boldsymbol{\Phi}_{j,\boldsymbol{k}_1,\boldsymbol{k}_2}^{SM_S(-)^*}(0,1,2), \tag{28}$$

where $\boldsymbol{\Phi}_{j,\boldsymbol{k}_1,\boldsymbol{k}_2}^{SM_S(-)}$ is an asymptotic approximation for the final-state wave function with two continuum electrons and $j \equiv (\gamma, s_j)$ where γ is the final state of the He^+ ion and s_j is the spin of the two continuum electrons. While Eq. (28) is strictly

only applicable for short-range potentials, ECS calculations for e-H collisions [27] demonstrated that the divergent phase of this integral formulation did not impact practical calculations for ionization cross sections. A formal justification for this has been given by Kadyrov *et al.* [28,29], which also shows that $z_1 = z_2 = 1$ is the optimum choice for the charges for the continuum waves. This integral method for single ionization was also used by Horner *et al.* [13] in their time-dependent implementation of the ECS method for this S-wave model.

For the excitation scattering outlined in the previous section the amplitudes are calculated using a fully antisymmetrized final-state wave function and evaluated on the surface of a hypercube. Here, to align more closely with the PECS electron-hydrogen Eqs. [2], a different but equivalent approach is taken; the final state is antisymmetrized w.r.t. the continuum electrons only and it is assumed that r_0 remains bound. As there is equal probability that r_0, r_1, or r_2 remains bound during single ionization, a factor of $\sqrt{3}$ is introduced into the amplitude, increasing the cross section by a factor of 3. We also note that the singlet and triplet configuration of the outgoing continuum waves are distinguishable and are summed incoherently in Eq. (38). The single-ionization amplitude is then calculated over a hypercylindrical surface using

$$\boldsymbol{F}^S_{ji}(\boldsymbol{k}_1,\boldsymbol{k}_2) \underset{\rho\to\infty}{\sim} \frac{\sqrt{3}\,\rho}{2(2\pi)^{5/2}} \int d\boldsymbol{r}_0 \int d\hat{\boldsymbol{r}}_1 \int d\hat{\boldsymbol{r}}_2 \int_0^{\pi/2} d\alpha \times r_1^2 r_2^2 \left[\boldsymbol{\Phi}^{SM_S(-)^*}_{j,\boldsymbol{k}_1,\boldsymbol{k}_2}(0,1,2) \frac{\partial}{\partial\rho} \boldsymbol{\Psi}^{SM_S}_i(0,1,2) - \boldsymbol{\Psi}^{SM_S}_i(0,1,2) \frac{\partial}{\partial\rho} \boldsymbol{\Phi}^{SM_S(-)^*}_{j,\boldsymbol{k}_1,\boldsymbol{k}_2}(0,1,2) \right], \tag{29}$$

where in six-dimensional hyperspherical coordinates

$$r_1 = \rho \sin\alpha, \tag{30}$$

$$r_2 = \rho \cos\alpha, \tag{31}$$

$$\rho = \sqrt{r_1^2 + r_2^2}, \tag{32}$$

and

$$d\boldsymbol{S} = \rho^5 \sin^2\alpha \cos^2\alpha \; d\alpha d\hat{\boldsymbol{r}}_1 d\hat{\boldsymbol{r}}_2 = \rho \; r_1^2 r_2^2 \; d\alpha d\hat{\boldsymbol{r}}_1 d\hat{\boldsymbol{r}}_2. \tag{33}$$

The final-state scattering wave function is approximated by

$$\boldsymbol{\Phi}^{SM_S(-)}_{j,\boldsymbol{k}_1,\boldsymbol{k}_2}(0,1,2) \sim \boldsymbol{\Phi}_\gamma(\boldsymbol{r}_0) \frac{1}{\sqrt{2}} \left[\boldsymbol{\Phi}^{(-)}_{\boldsymbol{k}_1}(\boldsymbol{r}_1) \boldsymbol{\Phi}^{(-)}_{\boldsymbol{k}_2}(\boldsymbol{r}_2) + (-1)^{s_j} \boldsymbol{\Phi}^{(-)}_{\boldsymbol{k}_1}(\boldsymbol{r}_2) \boldsymbol{\Phi}^{(-)}_{\boldsymbol{k}_2}(\boldsymbol{r}_1) \right] \chi_{s_j SM_S}(0,1,2), \tag{34}$$

where $\boldsymbol{\Phi}_\gamma(\boldsymbol{r}_0)$ is the He^+ final-state wave function and $\boldsymbol{\Phi}^{(-)}_{\boldsymbol{k}}(\boldsymbol{r})$ are the chosen one-dimensional continuum waves with momentum $\boldsymbol{k}$. Due to orthogonality of the spin functions, only $\boldsymbol{\Psi}^{SM_S}_{i,s_j}$ contributes to the amplitude on the selected surface, and as $\boldsymbol{\Phi}^{SM_S(-)}_{j,\boldsymbol{k}_1\boldsymbol{k}_2}(0,1,2)$ and $\boldsymbol{\Psi}^{SM_S}_{i,s_j}(0,1,2)$ have the same $(\boldsymbol{r}_1,\boldsymbol{r}_2)$ symmetry, the final-state wave function can be simplified to

$$\boldsymbol{\Phi}^{SM_S(-)}_{j,\boldsymbol{k}_1,\boldsymbol{k}_2}(0,1,2) \sim \sqrt{2}\boldsymbol{\Phi}_\gamma(\boldsymbol{r}_0) \boldsymbol{\Phi}^{(-)}_{\boldsymbol{k}_1}(\boldsymbol{r}_1) \times \boldsymbol{\Phi}^{(-)}_{\boldsymbol{k}_2}(\boldsymbol{r}_2) \chi_{s_j SM_S}(0,1,2). \tag{35}$$

Formally, the divergence theorem that is used to derive (29) from the volume integral in (28) requires a closed surface. However, a "cap" on the hypercylinder at $r_0 = R_0$ can be neglected as $\boldsymbol{\Phi}_\gamma(\boldsymbol{r}_0)$ approaches zero for large r_0. In practice the r_0 integration can be limited to relatively small values ($0 \leqslant r_0 \lessapprox 2n_j^2$ for He^+ residual ions) without significantly impacting accuracy.

For the S-wave model with a neutral target the single-ionization amplitude reduces to

$$F^S_{ji}(k_1,k_2) \underset{\rho\to\infty}{\sim} \frac{2\sqrt{3}\,\rho}{\sqrt{\pi}k_1k_2} \int dr_0 \, \phi_\gamma(r_0) \int_0^{\pi/2} d\alpha \times \left[\phi_{k_1}(r_1)\phi_{k_2}(r_2) \frac{\partial}{\partial\rho} \tilde{\psi}^{SM_S}_{i,s_j}(r_0,r_1,r_2) - \tilde{\psi}^{SM_S}_{i,s_j}(r_0,r_1,r_2) \frac{\partial}{\partial\rho} \phi_{k_1}(r_1)\phi_{k_2}(r_2) \right]. \tag{36}$$

Several choices for the continuum waves $\phi_k(r)$ are investigated, including helium *triplet static exchange* approximation, helium *static* approximation, and a regular hydrogenic Coulomb wave with $z = 1$. The results from using these different continuum waves are discussed in detail in Sec. III. Unfortunately there is no known form for (35), constructed from single-electron functions, that is orthogonal to the ground and excited states of the target helium atom. Therefore, the flux from the non-breakup channels interferes with the single-ionization amplitudes, significantly affecting their accuracy. Horner *et al.* [13] countered this problem by subtracting an asymptotic approximation of these non-breakup channels from the scattering wave function. This method is also used in the PECS implementation by replacing $\psi^{SM_S}_{i,s_j}$ with

$$\tilde{\psi}^{SM_S}_{i,s_{12}}(r_0,r_1,r_2) = \psi^{SM_S}_{i,s_{12}}(r_0,r_1,r_2) - \frac{1}{\sqrt{3}} \sum_{j'}^{j'_{\max}} F^S_{j'i} \left[\delta_{s_{j'}s_{12}} e^{ik_{j'}r_0} \phi_{j'}(r_1,r_2) - \alpha^{s_{j'}s_{12}S}_{01} e^{ik_{j'}r_1} \phi_{j'}(r_0,r_2) - \alpha^{s_{j'}s_{12}S}_{02} e^{ik_{j'}r_2} \phi_{j'}(r_1,r_0) \right], \tag{37}$$

where j' represents a bound state of helium with spin $s_{j'}$ and $k_{j'}$ is the momentum of the scattered electron in this channel. Unless otherwise indicated, the calculations presented in this article subtract the $1sns$ singlet and triplet states of helium for $n \leqslant n_{\max} = 3$.

The energy-differential single-ionization cross section for the S-wave model is

$$\frac{d\,\sigma^S_{\gamma i}(k_1,k_2)}{d\epsilon_1} = \frac{2S+1}{2(2s_i+1)} \frac{k_1k_2}{k_i} \sum_{s_j} \left| F^S_{ji}(k_1,k_2) \right|^2, \tag{38}$$

where ϵ_1 is the energy of one of the outgoing electrons. The total single-ionization cross section is then evaluated using

$$\sigma^S_{\gamma i} = \int_0^{\epsilon/2} \frac{d\,\sigma^S_{\gamma i}(k_1,k_2)}{d\epsilon_1} d\epsilon_1, \tag{39}$$

where ϵ is the excess energy above the single-ionization threshold.

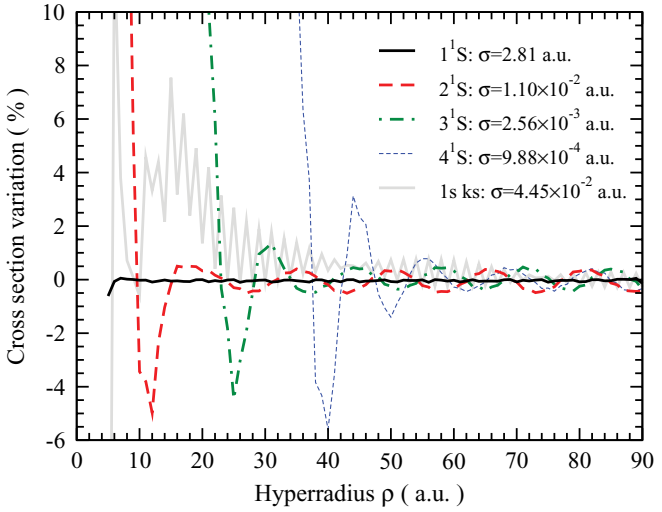

FIG. 4. (Color online) Convergence of single-excitation and single-ionization cross sections w.r.t. the hyperradius (ρ), expressed as a percentage variation from $\rho \approx 90$ a.u. calculations, for $E_0 = 53.9$ eV and ground-state target. The converged cross sections of these final states are shown in the legend.

F. Cross-section convergence and mesh size

One advantage of ECS-based methods is that the theoretical formulation of the scattering wave function has no significant approximations and is calculated to high accuracy over the entire (real) mesh. Thus, any hyperradius $0 < \rho \leqslant R_0$ can be used for the surface integrals in (26) and (36) allowing their radial-convergence behavior to be observed and giving a first-order approximation of the error associated with applying the asymptotic approximations for the final-state wave functions at a finite hyperradius. This generally gives the largest contribution to the numerical errors associated with ECS-based calculations. The convergence of the first few singlet scattering channels and the single-ionization channel for a 53.9-eV incident electron is presented in Fig. 4. The rate of convergence of these calculations is very similar to that observed for PECS e-H calculations [2], where the highly excited states require the largest ρ to converge, generally requiring $\rho \approx 4n_j^2$ a.u. for convergence to better than $\pm 1\%$.

For total (not differential) cross sections the standard error of the calculations undertaken for this article are estimated to be better than $\pm 2\%$, including numerical errors from the scattering wave function calculations. Radial convergence of the ionization channel is slower at lower energies and a larger mesh is needed (with wider mesh spacing), conversely a smaller mesh is needed at high energies (with finer spacing). For the calculations in this article the mesh size ranged from 200 a.u. for $E_0 = 5$ eV calculations to 25 a.u. for $E_0 = 500$ eV, though all calculations used a similar number of mesh points ($\approx$150 in each dimension) and hence computer time. Several calculations were undertaken with a large mesh ($\approx$250 points in each dimension).

III. RESULTS

The results for elastic and single-excitation scattering from a ground-state target are presented in Fig. 5 for incident

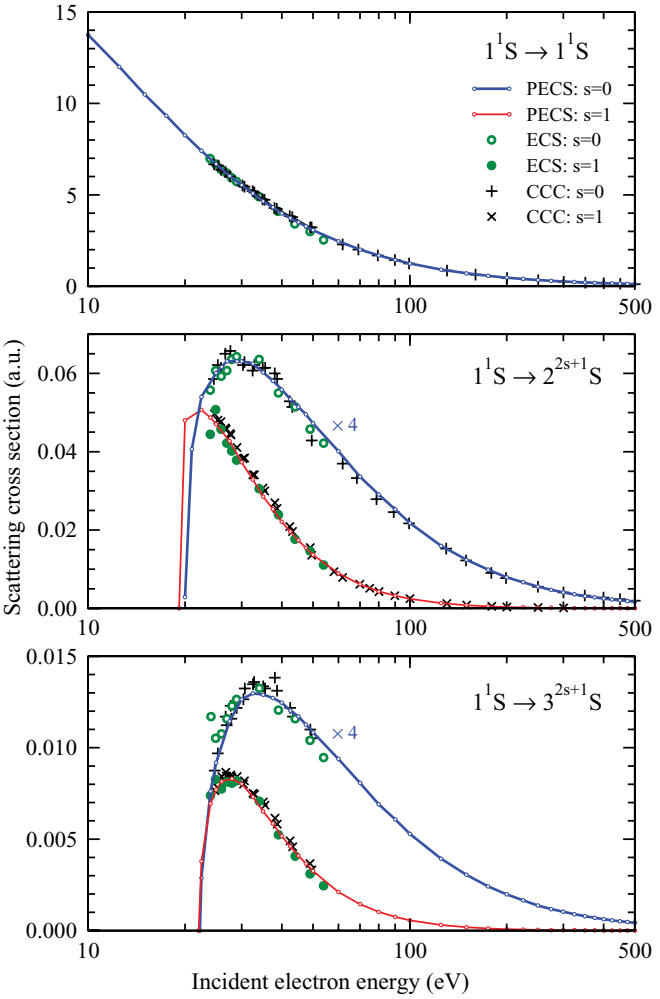

FIG. 5. (Color online) Total cross sections for electron-impact single excitation of a ground-state helium target in the S-wave model for 10- to 500-eV incident electron energies. TD-ECS [13] and CCC calculations [6,12] are also included.

electron energies ranging between 10 and 500 eV. The PECS results are generally in very good agreement with TD-ECS and CCC calculations, and a notable feature is the smoothness of the PECS curves, suggesting that the calculations are of high quality. The ECS results in this figure appear to show a systematic deviation from PECS at higher energies and exhibit an occasional outlier at lower energies. Both TD-ECS and PECS use similar surface integral techniques to evaluate these cross sections, the difference between the calculations is therefore most likely due to the scattering wave function calculation, which in TD-ECS calculations incorporates a Fourier transform to reconstruct the time-independent scattering wave function from the time-dependent wave packets. The variations, however, are not large. The CCC calculations also exhibit a small amount of scatter about the PECS results.

In Fig. 6 the elastic and single-excitation cross sections are shown for excited-state targets. Once again the PECS results are mostly in very good agreement with TD-ECS and CCC calculations, with the PECS calculations exhibiting a relatively smooth energy dependence. However, there is a moderate

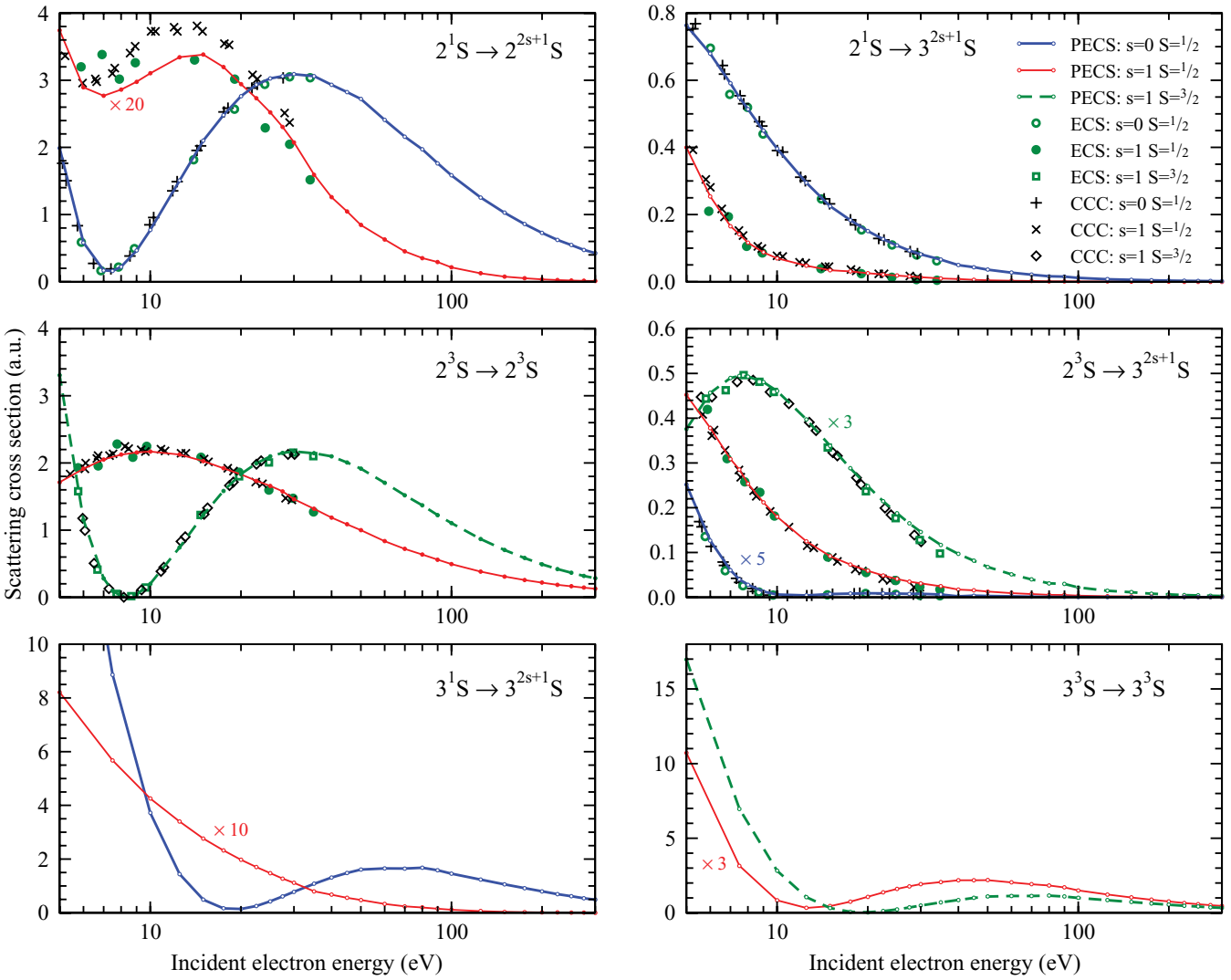

FIG. 6. (Color online) Total cross sections for electron-impact single excitation of an excited helium target in the S-wave model at 5- to 500-eV incident electron energies. TD-ECS [13] and CCC calculations [6,12] are also included.

variation between PECS and CCC near the peak of the $2^1S \rightarrow 2^3S$ cross section. The TD-ECS results tend to support the PECS calculations in this region. A notable feature of all these calculations is the significant suppression of the cross section in the 5- to 20-eV region for some of the transitions. It is not known if this feature has physical significance or if it is an unphysical artifact of the S-wave model.

Before the single-ionization results are presented it is important to examine the effect that the different choices for the continuum waves $\phi_k(r)$ in (36) have upon them, along with the impact of asymptotic subtraction [see Eq. (37)] of non-breakup channels from the scattering wave function. In their TD-ECS calculations, Horner *et al.* [13] used the helium triplet static exchange approximation to evaluate the continuum waves (He^3_{exch}) for single ionization. These are orthogonal to the $He^+(1s)$ orbital and approximately orthogonal to the helium excited-state orbitals. They are not, however, orthogonal to the helium ground state. As the flux from different channels overlaps in coordinate space, orthogonality of the continuum waves to the helium bound wave functions is required to accurately separate the amplitudes of the different channels. Without this orthogonality (and there are no known single-coordinate continuum functions that satisfy this requirement) flux from non-breakup channels will interfere with the ionization amplitude calculations. Therefore, it is important (as the elastic channel has by far the greatest flux) that the non-breakup channels are subtracted accurately from the scattering wave function to prevent this interference. For our calculations we used the formulation of these continuum waves that is developed in [30].

The energy-differential single-ionization cross sections for ground-state helium with $E_0 = 53.9$ eV are shown in Fig. 7 with various choices for the continuum wave and number of non-breakup channels (n_{max}) subtracted (where n refers to the $1sns$ singlet and triplet states). The light gray dashed curve in Fig. 7(a) shows the dramatic effect of using He^3_{exch} without subtraction, it is highly oscillatory and grossly overestimates the cross section.

As an alternative to He^3_{exch} waves we have chosen to use the helium static approximation (without exchange) for the continuum waves (He_{st}). These are calculated using a procedure similar to that outlined in [30], but excluding the

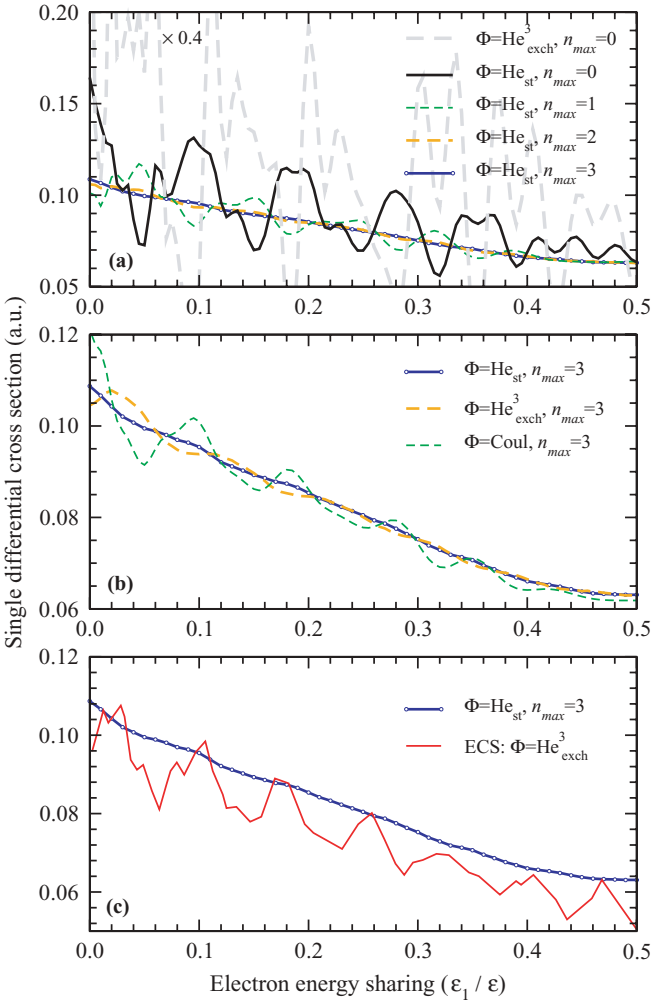

FIG. 7. (Color online) SDCS for electron-impact single ionization of ground-state helium in the S-wave model at 53.9-eV incident electron energy. (a) PECS calculations using various $n_{\max}$ for asymptotic subtraction. (b) PECS calculations using He_{st}, He^3_{exch}, and Coulomb ($z = 1$) continuum waves. (c) PECS calculation using helium static continuum waves (He_{st}) compared with a TD-ECS calculation [13] using helium triplet static exchange (He^3_{exch}) continuum waves.

iterative procedure used to incorporate exchange (that is setting $g = 0$ in Eq. (24) of that article). In Fig. 7(a) we see that, without subtraction ($n_{\max} = 0$), this continuum wave gives results with much smaller oscillations that are reasonably close to the converged results. This suggests that this continuum wave is approximately orthogonal to the helium ground state, greatly reducing the interference from the elastic channel. The remainder of the curves in Fig. 7(a) show the convergence of the results w.r.t. increasing the number of channels subtracted. Generally, we use $n_{\max} = 3$ as convergence of the higher single-excitation channels requires larger R_0 and the small increase in accuracy does not warrant the large increase in computational effort this requires.

After subtraction of the non-breakup channels we would expect that He^3_{exch} and He_{st} continuum waves will give similar results. In Fig. 7(b) we show these along with a regular Coulomb wave (with $z = 1$). There appears to be a definite advantage in using He_{st} waves, though this benefit was observed to diminish at energies closer to threshold.

Figure 7(c) shows the converged PECS single-differential cross section (SDCS) results at 53.9 eV that compares favorably with a TD-ECS calculation by Horner *et al.* [13]. The TD-ECS calculation, however, contains oscillations that are larger than those expected from using He^3_{exch} continuum waves, as shown in Fig. 7(b). This suggests that the TD-ECS scattering wave function at this energy has not completely converged, or perhaps an additional error has been introduced through their Fourier transformation process (which is not required in these time-independent calculations). We note that no S-wave energy-differential cross sections have been published for the CCC [6] method.

To smooth the oscillations in the TD-ECS energy-differential results, Horner *et al.* [13] performed a least-squares fit to a quadratic equation. The underlying assumption in this decision is that the model SDCSs have a "smile" shape (symmetric about equal energy sharing) similar to the SDCS of the full helium system and readily approximated by a quadratic equation. For the Temkin-Poet model for e-H collisions,

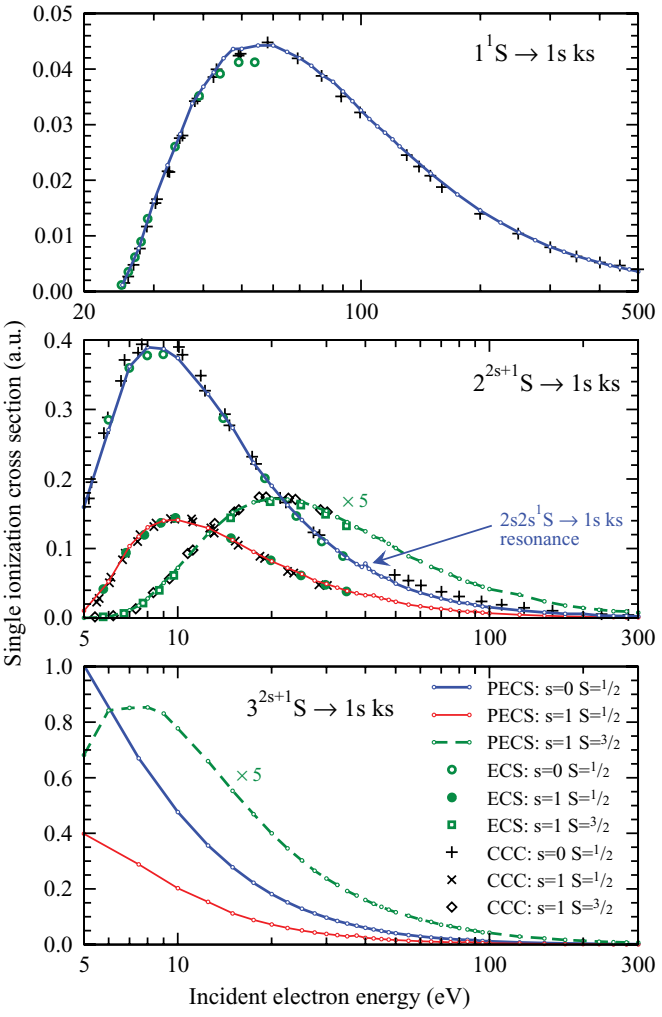

FIG. 8. (Color online) Total cross sections for electron-impact single ionization of ground-state and excited-state helium targets in the S-wave model at 5- to 500-eV incident electron energies. TD-ECS [13] and CCC [6,12] calculations are also included.

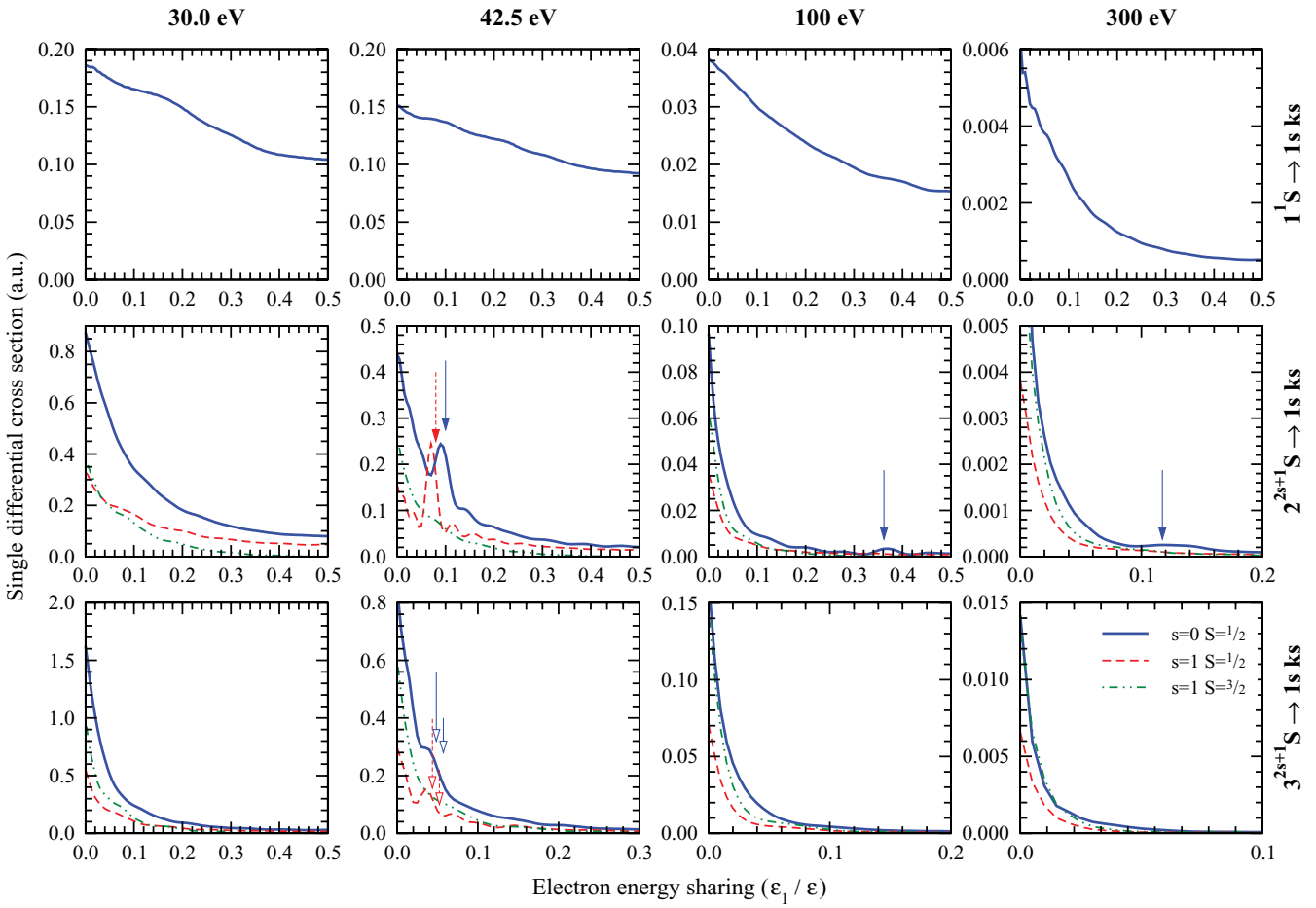

FIG. 9. (Color online) SDCS for electron-impact single ionization of ground- and excited-state helium targets in the S-wave model at 30- to 300-eV incident electron energies. Autoionization energies are shown with solid long arrows for $2s2s^1S \rightarrow 1sks$ (34.75 eV), empty long arrows for $2s3s^1S \rightarrow 1sks$ (38.86 eV), and empty short arrows for $2s3s^3S \rightarrow 1sks$ (38.51 eV).

Bartlett and Stelbovics ([31], Fig. 10) demonstrated that rather than a concave "smile" shape, this model had a slightly convex shape, and indeed even at very large hyperradii (1400 a.u.) complete convergence of the results near equal-energy sharing could not be obtained. This behavior was attributed to the nonanalytic nature of the electron-electron potential of the model, which has a discontinuous first derivative at $r_1 = r_2$. This S-wave model for helium also has nonanalytic electron-electron potentials, and while undertaking 1400 a.u. calculations is well beyond current computational resources, similar convergence behavior with increasing ρ was observed in the PECS results for e-He. Consequently, smoothing the energy-differential cross sections using a quadratic equation may not be valid for this model, especially at higher incident energies. Consequently, no smoothing of any PECS results is undertaken in this article.

The total single-ionization cross sections for ground- and excited-state targets are plotted in Fig. 8 for energies from threshold to 500 eV (300 eV for excited targets). They exhibit the characteristic single-peak structure exhibited by the single-ionization of most atoms, and the results are in excellent agreement with TD-ECS and CCC results, though the TD-ECS calculations for a ground-state target appear to show a slight systematic deviation near the peak of the cross section. The PECS results exhibit a very smooth energy dependence, with the exception of a very small peak in the $1s2s^1S$ excited-state target results near $E_0 = 40$ eV ($\epsilon = 36.1$ eV). This peak is due to the $2s2s^1S \rightarrow 1sks$ autoionizing transition that has an energy of 34.75 eV. This interference structure was observed in the energy-differential TD-ECS calculations and discussed in detail in a very interesting article by Horner *et al.* [14]. The accuracy of the PECS calculations allows this interference feature to be resolved in the integrated cross sections. There also appear to be slight outliers at similar energies in the other PECS excited-state calculations, though these are yet to be confirmed (in the total cross sections) to be due to interference from the autoionization channels.

Finally, we present energy-differential single-ionization cross sections for ground- and excited-state targets in Fig. 9 at some representative energies: $E_0 = 30.0$, 42.5, 100, and 300 eV. At higher incident energies the energy-sharing of the outgoing electrons becomes increasingly asymmetric, a common feature of the single-ionization cross section of atoms. It should be noted that in the higher-energy plots for the excited targets that the x-axis range has been reduced so as to give more detail for these high-slope, narrow peaks. Two low-energy results (30.0 and 42.5 eV) are shown, selected to be below and above the onset of autoionization. The

energies of these interference features are shown with arrows, noting that two peaks are present (at ϵ_1 and $1-\epsilon_1$) as the energy-differential cross sections are symmetric about equal-energy sharing, though we only display the lower half. Also, the same autoionization energy appears at different positions depending on the target's single-ionization energy.

The *near-threshold* autoionization interference peaks shown in Fig. 9 were calculated using TD-ECS for $2^{2s+1}S$ and $3^{2s+1}S$ targets and are discussed in detail in [14]. Somewhat unexpectedly, however, the PECS calculations also reveal structure in the energy-differential cross sections due to $2s2s^1S$ autoionization at *high* incident energies (100 and 300 eV), significantly above their threshold energy. The interference structure broadens significantly with increasing energy.

IV. CONCLUSION

In this article we have developed the theoretical and computational framework for a four-body time-independent PECS method and applied it to an S-wave model for electron-helium collisions. Results for elastic, single-excitation, and ionizing collisions were presented for a large range of energies and initial target states and compared with CCC and TD-ECS calculations. There was generally good agreement between these methods, while the PECS results were notable for their smooth curves for both total and energy-differential cross sections where oscillations and outliers were within the estimated standard error of 2% and evidence of their benchmark quality. The stability of the PECS calculations is also evidenced by the small autoionization interference feature that was resolved in the total single-ionization cross sections for the $1s2s^1S$ excited-state target.

In the sequel to this article [22] we present PECS calculations for the four-body processes open to the S-wave model for helium. Along with the three-body results given here, we demonstrate that the PECS method is able to resolve all the channels open to electron-helium scattering to high precision. This bodes well for the future application of the PECS method to the full electron-helium collision system.

ACKNOWLEDGMENTS

We acknowledge the Australian Research Council for funding this research and the National Computational Infrastructure Facility for providing supercomputing facilities.

APPENDIX: ANTISYMMETRIZATION

The antisymmetrization operator for a three-electron system may be given as

$$\mathcal{A} = \frac{1}{\sqrt{3!}\sqrt{N!}}(1 - P_{01} - P_{02} - P_{12} + P_{01}P_{12} + P_{02}P_{12}), \tag{A1}$$

where P_{ij} is the permutation operator that permutes both space and spin coordinates of i and j. The normalization constant N depends on the antisymmetrization and normalization already applied to wave function that the operator acts upon: $N = 1$ if the operator acts upon a wave function that has no antisymmetrization, $N = 2$ if it is symmetric w.r.t. exchange of a *single* pair of coordinates, and $N = 3$ if it is already antisymmetric w.r.t. exchange of *any* pairs of the coordinates.

In this article the helium wave functions are already normalized and antisymmetrized w.r.t. exchange of their electrons. For equations that include the helium wave function the antisymmetrization operator becomes

$$\mathcal{A} = \frac{1}{\sqrt{3}}(1 - P_{01} - P_{02}). \tag{A2}$$

The symmetry of the radial wave functions, tripolar spherical harmonic functions, and spin functions, w.r.t. exchange of particles, can be evaluated from first principles using general tensor relations (see [32]). For the S-wave model considered in this article, where all orbital angular momenta are zero, the space-permutation functions reduce to unity and the symmetry of the wave functions are determined solely from the spin-permutation functions. The spin function $\chi_{sSM_S}(\sigma_0, \sigma_1, \sigma_2)$ has total spin S, each electron has spin $1/2$, and we choose to couple the spins of electrons 1 and 2 to give the substate spin s, that is, $[0_{\frac{1}{2}} \otimes (1_{\frac{1}{2}} \otimes 2_{\frac{1}{2}})_s]_S$.

Applying general tensor relations gives the symmetries

$$\chi_{sSM_S}(102) = \sum_{s'} \alpha_{01}^{ss'S}\ \chi_{s'SM_S}(012), \tag{A3}$$

$$\chi_{sSM_S}(210) = \sum_{s'} \alpha_{02}^{ss'S}\ \chi_{s'SM_S}(012), \tag{A4}$$

$$\chi_{sSM_S}(021) = (-1)^s \chi_{sSM_S}(012), \tag{A5}$$

where

$$\alpha_{01}^{ss'S} = -(-1)^{s-s'}\hat{s}\hat{s}' \begin{Bmatrix} \frac{1}{2} & \frac{1}{2} & s \\ S & \frac{1}{2} & s' \end{Bmatrix}, \tag{A6}$$

$$\alpha_{02}^{ss'S} = -\hat{s}\hat{s}' \begin{Bmatrix} \frac{1}{2} & \frac{1}{2} & s \\ S & \frac{1}{2} & s' \end{Bmatrix}, \tag{A7}$$

and $\hat{s} = \sqrt{2s+1}$.

The remaining symmetry relations can be constructed through a combination of the spin-permutation functions, giving

$$\chi_{sSM_S}(120) = \sum_{s'} \alpha_{01}^{ss'S}\ (-1)^{1-s'}\ \chi_{s'SM_S}(012), \tag{A8}$$

$$\chi_{sSM_S}(201) = \sum_{s'} \alpha_{02}^{ss'S}\ (-1)^{1-s'}\ \chi_{s'SM_S}(012). \tag{A9}$$

These spin-function symmetry relations are consistent with those presented in [33].

[1] P. L. Bartlett, A. T. Stelbovics, and I. Bray, J. Phys. B **37**, L69 (2004).
[2] P. L. Bartlett, J. Phys. B **39**, R379 (2006).
[3] D. V. Fursa and I. Bray, Phys. Rev. A **52**, 1279 (1995).
[4] K. Bartschat, E. T. Hudson, M. P. Scott, P. G. Burke, and V. M. Burke, Phys. Rev. A **54**, R998 (1996).

[5] M. S. Pindzola and F. J. Robicheaux, Phys. Rev. A **61**, 052707 (2000).
[6] C. Plottke, I. Bray, D. V. Fursa, and A. T. Stelbovics, Phys. Rev. A **65**, 032701 (2002).
[7] M. S. Pindzola, F. J. Robicheaux, J. P. Colgan, M. C. Witthoeft, and J. A. Ludlow, Phys. Rev. A **70**, 032705 (2004).
[8] M. S. Pindzola, F. Robicheaux, and J. P. Colgan, J. Phys. B **41**, 235202 (2008).
[9] M. Dürr, A. Dorn, J. Ullrich, S. P. Cao, A. Czasch, A. S. Kheifets, J. R. Götz, and J. S. Briggs, Phys. Rev. Lett. **98**, 193201 (2007).
[10] X. Ren, A. Dorn, and J. Ullrich, Phys. Rev. Lett. **101**, 093201 (2008).
[11] M. S. Pindzola, D. Mitnik, and F. Robicheaux, Phys. Rev. A **59**, 4390 (1999).
[12] C. Plottke, P. Nicol, I. Bray, D. V. Fursa, and A. T. Stelbovics, J. Phys. B **37**, 3711 (2004).
[13] D. A. Horner, C. W. McCurdy, and T. N. Rescigno, Phys. Rev. A **71**, 012701 (2005).
[14] D. A. Horner, C. W. McCurdy, and T. N. Rescigno, Phys. Rev. A **71**, 010701(R) (2005).
[15] A. Temkin, Phys. Rev. **126**, 130 (1962).
[16] R. Poet, J. Phys. B **11**, 3081 (1978).
[17] T. N. Rescigno, M. Baertschy, W. A. Isaacs, and C. W. McCurdy, Science **286**, 2474 (1999).
[18] C. W. McCurdy, M. Baertschy, and T. N. Rescigno, J. Phys. B **37**, R137 (2004).
[19] P. L. Bartlett, A. T. Stelbovics, and I. Bray, Phys. Rev. A **68**, 030701(R) (2003).
[20] P. L. Bartlett and A. T. Stelbovics, Phys. Rev. Lett. **93**, 233201 (2004).
[21] J. F. Williams, P. L. Bartlett, and A. T. Stelbovics, Phys. Rev. Lett. **96**, 123201 (2006).
[22] P. L. Bartlett and A. T. Stelbovics, Phys. Rev. A **81**, 022716 (2010).
[23] C. W. McCurdy, T. N. Rescigno, and D. Byrum, Phys. Rev. A **56**, 1958 (1997).
[24] T. N. Rescigno, M. Baertschy, D. Byrum, and C. W. McCurdy, Phys. Rev. A **55**, 4253 (1997).
[25] M. Draeger, G. Handke, W. Ihra, and H. Friedrich, Phys. Rev. A **50**, 3793 (1994).
[26] R. K. Peterkop, *Theory of Ionization of Atoms by Electron Impact* (Colorado Associated University Press, Boulder, CO, 1977).
[27] M. Baertschy, T. N. Rescigno, and C. W. McCurdy, Phys. Rev. A **64**, 022709 (2001).
[28] A. S. Kadyrov, A. M. Mukhamedzhanov, A. T. Stelbovics, and I. Bray, Phys. Rev. Lett. **91**, 253202 (2003).
[29] A. S. Kadyrov, I. Bray, A. M. Mukhamedzhanov, and A. T. Stelbovics, Ann. Phys. **324**, 1516 (2009).
[30] I. Bray and D. V. Fursa, Phys. Rev. A **54**, 2991 (1996).
[31] P. L. Bartlett and A. T. Stelbovics, Phys. Rev. A **69**, 022703 (2004).
[32] D. A. Varshalovich, A. N. Moskalev, and V. K. Khersonskii, *Quantum Theory of Angular Momentum* (World Scientific Publishing, Singapore, 1988).
[33] A. T. Stelbovics and L. Berge, Phys. Rev. A **55**, 1028 (1997).